Optics Letters

Angle-resolved multioctave supercontinua from mid-infrared laser filaments

A. V. Mitrofanov,[1,2,3,4] A. A. Voronin,[1,2] D. A. Sidorov-Biryukov,[1,2] S. I. Mitryukovsky,[1] M. V. Rozhko,[1,2] A. Pugžlys,[5] A. B. Fedotov,[1,2] V. Ya. Panchenko,[3,4] A. Baltuška,[5] and A. M. Zheltikov[1,2,3,6,*]

[1]Russian Quantum Center, ul. Novaya 100, Skolkovo, Moscow Region 143025, Russia
[2]Physics Department, International Laser Center, M.V. Lomonosov Moscow State University, Moscow 119992, Russia
[3]Kurchatov Institute National Research Center, Moscow 123182, Russia
[4]Institute of Laser and Information Technologies, Russian Academy of Sciences, Shatura, Moscow Region 140700, Russia
[5]Photonics Institute, Vienna University of Technology, Gusshausstrasse 27-387, 1040 Vienna, Austria
[6]Department of Physics and Astronomy, Texas A&M University, College Station, Texas 77843, USA
*Corresponding author: zheltikov@physics.msu.ru

Received 25 April 2016; revised 12 June 2016; accepted 13 June 2016; posted 14 June 2016 (Doc. ID 263912); published 21 July 2016

Angle-resolved spectral analysis of a multioctave high-energy supercontinuum output of mid-infrared laser filaments is shown to provide a powerful tool for understanding intricate physical scenarios behind laser-induced filamentation in the mid-infrared. The ellipticity of the mid-infrared driver beam breaks the axial symmetry of filamentation dynamics, offering a probe for a truly (3 + 1)-dimensional spatiotemporal evolution of mid-IR pulses in the filamentation regime. With optical harmonics up to the 15th order contributing to supercontinuum generation in such filaments alongside Kerr-type and ionization-induced nonlinearities, the output supercontinuum spectra span over five octaves from the mid-ultraviolet deep into the mid-infrared. Full (3 + 1)-dimensional field evolution analysis is needed for an adequate understanding of this regime of laser filamentation. Supercomputer simulations implementing such analysis articulate the critical importance of angle-resolved measurements for both descriptive and predictive power of filamentation modeling. Strong enhancement of ionization-induced blueshift is shown to offer new approaches in filamentation-assisted pulse compression, enabling the generation of high-power few- and single-cycle pulses in the mid-infrared.

OCIS codes: (190.7110) Ultrafast nonlinear optics; (260.7120) Ultrafast phenomena.

http://dx.doi.org/10.1364/OL.41.003479

Laser-induced filamentation [1–3] remains one of the hot topics in ultrafast optical physics, continuing to attract much attention as an intriguing manifestation of nonlinear wave dynamics [2,3] and finding growing applications as a pulse-compression technology for high-peak-power optical fields [4,5], a method of high-energy beam delivery and high-brightness supercontinuum generation [6], as well as a promising approach for the remote sensing of the atmosphere [7]. Recent experimental studies [8–11] demonstrate that optical technologies based on laser filamentation can be advantageously extended to the mid-infrared. Filamentation of ultrashort mid-IR pulses offers a powerful source of high-energy multioctave, mid-ultraviolet-to-mid-infrared supercontinua [8–10], enables efficient compression of high-power pulses in the mid-IR [11], helps increase the energy of laser pulses transmitted through the atmospheric air [9], and opens new horizons in standoff detection and remote sensing [12].

Laser filamentation in the mid-infrared involves a broad class of nonlinear-optical phenomena that do not show up in visible and near-infrared filaments. The most prominent examples include generation of multiple odd-order harmonics [10] and strong plasma refraction [9], which tends to give rise to ring-shaped beam patterns, especially well-resolved toward the back of the pulse, as well as a shift in the balance between the self-focusing due to the Kerr effect and plasma-induced defocusing. With all these effects manifested in the inherently off-axial beam dynamics [9,10], angle-resolved studies on the supercontinuum filament output have to be included as an essential tool needed to understand laser filaments in the mid-infrared. Because such angle-resolved measurements have to be performed within a bandwidth of several octaves, stretching from the ultraviolet deep into the mid-infrared, multiple challenges need to be confronted in implementing experimental methods that would enable such studies.

Here, we address these challenges by presenting an experimental approach for angle-resolved studies on a multioctave high-energy supercontinuum output of laser filaments induced in atmospheric air by 0.25 TW, 3.9 μm driver pulses. With optical harmonics up to the 15th order contributing to supercontinuum generation alongside Kerr-type and ionization-induced nonlinearities, the spectra of this supercontinuum radiation span over almost five octaves from the ultraviolet deep into the mid-infrared spectral range. As we demonstrate below, rewards for such angle-resolved measurements are numerous. Performed on an ultrabroadband beam, these studies reveal clearly resolved signatures of a complex off-axial beam dynamics, which is intrinsic to laser filamentation in the mid-infrared, as opposed to near-infrared filaments, thus offering important insights into an intricate and in many ways unusual spatiotemporal evolution of high-power mid-infrared pulses in the filamentation regime.

High-power ultrashort mid-IR driver pulses are delivered in our experiments by a laser system (Fig. 1) consisting of a solid-state ytterbium laser with an amplifier, a three-stage optical parametric amplifier (OPA), a grating–prism (grism) stretcher, a Nd: YAG pump laser, a three-stage optical parametric chirped-pulse amplification (OPCPA) system, and a grating compressor for mid-IR pulses [9,10]. The compressed-pulse idler-wave OPCPA output has a central wavelength of 3.9 μm, a pulse width of 80 fs, and an energy up to 30 mJ. Spectral measurements in the mid-IR range are performed with a homebuilt spectrometer consisting of a scanning monochromator and a thermoelectrically cooled HgCdTe detector (Fig. 1). For the spectral measurements in the ultraviolet, visible, and near-IR ranges, OceanOptics HR4000 and NIRQuest spectrometers were employed. Temporal envelopes and phases of mid-IR pulses are characterized using frequency-resolved optical gating based on second-harmonic generation in a 0.5 mm thick $AgGaS_2$ crystal. A typical spectrum of the 3.9 μm OPCPA output is shown by gray shading in Fig. 2(a).

The mid-IR OPCPA output beam has a shape of a 3 cm by 2 cm ellipse, which breaks the axial symmetry of filamentation [Figs. 2(b)–2(e)], providing a probe for a truly (3 + 1)-dimensional [(3 + 1) – d] spatiotemporal evolution of mid-infrared pulses in the filamentation regime. This beam is focused by a 0.5 m focal-length CaF_2 lens to induce a filament in the atmosphere, visualized by a bright spark and is accompanied by a generation of broadband, white-light radiation, whose spectrum continuously spans over at least 4.7 octaves, stretching from 250 to 6500 nm [Fig. 2(a)]. The high-frequency part of the supercontinuum is drastically enhanced by odd-order harmonics of the driver. Odd harmonics up to the 15th order are clearly seen in supercontinuum spectra in Fig. 2(a) as spectrally broadened, still well-resolved peaks near the frequencies $(2m + 1)\omega_0$, where m is an integer and ω_0 is the central frequency of the mid-infrared driver.

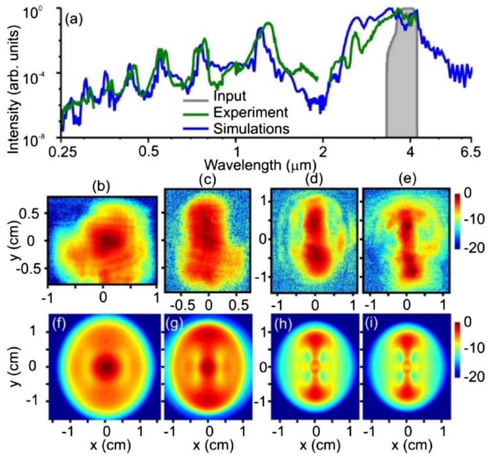

Fig. 2. (a) On-axis spectrum of supercontinuum radiation generated in a filament induced by the mid-IR OPCPA output in the air: (green) experiment, (blue) simulations. The spectrum of the mid-IR driver inducing the filament is shown with gray shading. (b)–(i) Far-field beam profiles of the supercontinuum output of the mid-IR filament: (b)–(e) experiments and (f)–(i) simulations. The filament is induced by 3.9 μm, 80 fs pulses with an energy of (b), (f) 4 mJ, (c), (g) 7 mJ, (d), (h) 11 mJ, and (e), (i) 17 mJ. The color scale encodes the normalized field intensity.

The angle-resolved spectral analysis of the supercontinuum output of mid-infrared filaments in our experiments was performed by measuring supercontinuum spectra behind an 0.8 mm pinhole, which was scanned in the direction orthogonal to the beam axis (Fig. 1). Angle-resolved spectral measurements reveal a complex, nonuniform distribution of spectral components over the supercontinuum beam [Fig. 3(a)]. As one of the most striking tendencies, the off-axial spectra display a strong blueshift relative to their on-axis counterparts. The mid-IR part of the spectrum is dominated by an intense feature that represents the broadened spectrum of the driver. Off the beam axis, this part of the spectrum is blue-shifted all the way up to 1.5 μm [Fig. 3(a)]. The off-axial harmonic signals are also

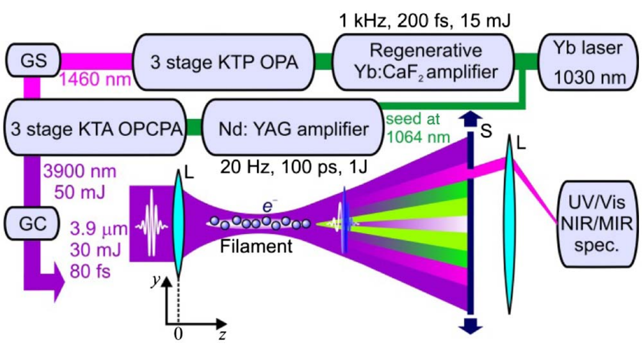

Fig. 1. Experimental setup: GS, grism stretcher; GC, grating compressor; L, lenses; UV/Vis/NIR/MIR spec., spectrometers for spectral analysis in the UV, visible, near-IR, and mid-IR ranges; S, screen with a pinhole.

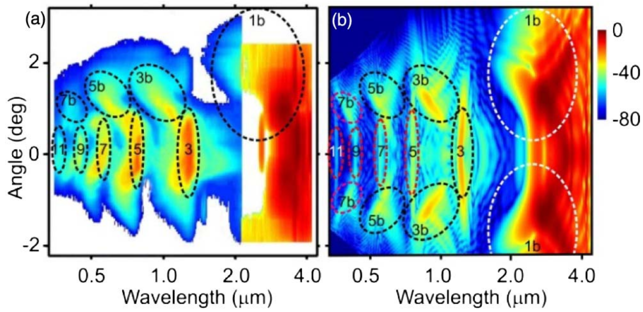

Fig. 3. Angle-resolved spectra of the supercontinuum output of the filament induced by 3.9 μm, 80 fs, 17 mJ driver pulses: (a) experiment and (b) simulations. Optical harmonics generated in the filament are labeled by numbers from 3 to 11, standing for the harmonic order. A letter "b" added to these numbers indicates the blueshifted component of the mth-order harmonic. The blueshifted off-axial components generated by the mid-infrared driver are labeled as 1b.

seen to be systematically blueshifted relative to their on-axis counterparts.

Because of the beam ellipticity of the mid-infrared driver in our experiments, simplified models of laser filamentation based on the assumption of an axially symmetric beam dynamics, become inapplicable, requiring full $(3+1)-d$ field evolution analysis. To address this problem, we use a model of laser filamentation based on the 3D time-dependent generalized nonlinear Schrödinger equation (GNSE) for the amplitude of the field, which is referred to hereinafter as the $(3+1)-d$ GNSE model:

$$\begin{aligned}\frac{\partial}{\partial z}\tilde{A} = &\left[\frac{ic}{2\omega n_0}\Delta_\perp + i\tilde{D}(\omega)\right]\tilde{A} + \tilde{F}\left[i\frac{\omega_0\tilde{T}}{c}[n_2(1-f_R)|A|^2\right.\\ &+ f_R\int_{-\infty}^{\infty}R(t-t')|A(t')|^2\mathrm{d}t' + n_4|A|^4]A\\ &\left.+ i\frac{\omega_0\mu_0\chi^{(3)}\tilde{T}}{4n_0^2}A^3 - \frac{U_iW(I)(\rho_0-\rho)}{2I}A\right]\\ &- \left(\frac{i\omega_0^2\omega}{2cn_0\rho_c(\omega^2+\tau_c^{-2})} + \frac{\sigma(\omega)}{2}\right)\tilde{F}[\rho(t)A].\end{aligned}$$

Here, $A \equiv A(t,x,y,z)$ is the field envelope, $\tilde{A} \equiv \tilde{A}(\omega,x,y,z)$ is its Fourier transform, $\Delta\perp = \partial^2/\partial x^2 + \partial^2/\partial y^2$, x, y are the transverse coordinates, z is the coordinate along the propagation axis, t is the retarded time, $\omega = 2\pi c/\lambda$ is the radiation frequency, λ is the wavelength, $\tilde{F}$ is the Fourier transform operator, $\tilde{D} = k(\omega) - k(\omega_0) - \partial k/\partial\omega|_{\omega o}(\omega-\omega_0)$, ω_0 is the central frequency, $k(\omega) = \omega n(\omega)/c$, $n(\omega)$ is the refractive index, $n_0 = n(\omega_0)$, n_2 and n_4 are the Kerr nonlinearity coefficients, $\chi^{(3)}$ is the nonlinear susceptibility responsible for four-wave mixing, $\tilde{T} = 1 + i\omega_0^{-1}\partial/\partial t$, $\rho \equiv \rho(t,x,y,z)$ is the electron density, ρ_0 is the neutral gas density, $\rho_c = \omega_0^2 m_e\epsilon_0/e^2$ is the critical electron density, $U_i = U_0 + U_{\mathrm{osc}}$, U_i is the ionization potential, U_{osc} is the energy of field-induced electron oscillations, $W(I)$ is the photoionization rate, $\sigma(\omega)$ is the impact ionization cross section, and e and m_e are the electron charge and mass, respectively.

This model includes all the key physical effects involved in laser filamentation, such as dispersion and absorption, beam diffraction, Kerr nonlinearities, pulse self-steepening, spatial self-action phenomena, as well as ionization-induced loss, dispersion, and optical nonlinearities. The field evolution equation in this model is solved jointly with the rate equation for the electron density, $\partial\rho/\partial t = W(\rho-\rho_0) + \sigma(\omega_0)U_i^{-1}\rho I$, which includes both photoionization and impact ionization, with the photoionization rate W calculated using the Keldysh formalism [13].

The need to include optical harmonics of the mid-IR driver up to the 15th order further increases the computational complexity of $(3+1)-d$ GNSE simulations. A typical $(3+1)-d$ grid needed to provide an adequate accuracy and robustness of numerical simulations includes a total of $4096 \times 512 \times 512 \times 10^4$ grid points along t, x, y, and z, translating into an overall complexity of the problem on the order of 0.5–1.0 exaflop. To run such simulations, we employed an MPI parallel programming interface and the CUDA graphical architecture on the supercomputer clusters at Moscow State University.

With a standard set of constants for the dispersion, nonlinearity, and ionization for the atmospheric air [2,3,11], numerical simulations accurately reproduce the angle-resolved supercontinuum spectra [cf. Figs. 3(a) and 3(b)], the supercontinuum beam profiles [Figs. 2(b)–2(i)], as well as on-axis supercontinuum spectra [Fig. 2(a)] within a spectral range of about five octaves. The filament length for our experimental conditions (≈3 cm) is ≈25 times longer than the Rayleigh length. Much longer filament lengths were achieved with looser beam focusing [9]. In Figs. 3(a) and 3(b), we compare experimental and simulated angle-resolved spectra of the supercontinuum output of the filament. Optical harmonics generated in the filament are labeled by numbers from 3 to 11, standing for the harmonic order. The off-axial components of the driver and harmonics experience strong ionization-induced blueshift. For these components, a letter "b" is added to their numbers, with mb, indicating the blueshifted component of the mth-order harmonic. The blueshifted off-axial components generated by the mid-infrared driver are labeled as 1b. Our $(3+1)-d$ simulations are seen to accurately describe the overall spectral broadening of the mid-IR driver, as well as the overall spectra of optical harmonics integrated over the beam [Figs. 2(a), 3(a), and 3(b)]. Moreover, both the on- and off-axis spectra of optical harmonics also are predicted with a reasonable accuracy [Figs. 3(a) and 3(b)]. The model also correctly describes the ionization-induced blueshift of the off-axial components of the driver field [1b in Figs. 3(a) and 3(b)] and its most intense, third to eleventh harmonics [3b, 5b, and 7b in Figs. 3(a) and 3(b)].

Such a close agreement between simulations and experimental results proves the predictive power of our (3 + 1)-dimensional physical and numerical model, validating this model as a tool to understand the physical scenarios of laser filamentation in the mid-infrared. These simulations show [Figs. 4(a)–4(d)] that, in the leading edge of the pulse [$\tau = -50$ fs in Fig. 4(b), τ being the time in the frame of reference related to the peak of the pulse], where the field intensity is low, self-focusing and ionization effects are negligible. However, as the field intensity increases toward the central part of the pulse, nonlinear phenomena and gas ionization become significant [Figs. 4(c) and 4(d)]. The central part of the mid-IR driver and its trailing edge undergo defocusing [Figs. 4(c) and 4(d)] by a transient electron-density gradient induced by the leading edge of the pulse (typically, about 80% of electron density is due to photoionization, with the remaining part induced by impact ionization). Strong interaction of this part of the beam with the plasma created by the leading edge of the pulse induces a dramatic blueshift, giving rise to intense conical features clearly seen in Fig. 4(e). This off-axial beam dynamics is distinctly different from conical wave emission and related x-wave dynamics, caused by parametric wave mixing in near-IR filaments [3]. In the mid-IR range, beam dynamics of this type are entirely due to ionization [Figs. 4(b)–4(d)]. It is never observed when ionization effects are switched off in simulations. Because of a relatively short focal length, shock-wave effects, which tend to become prominent within much longer propagation paths [14,15], do not play any noticeable role in our filamentation geometry. Moreover, because of plasma effects, self-steepening was observed in our beam geometry in the leading rather than in the trailing edge of the pulse, which would have been typical of shock-wave-dominated pulse evolution.

In the long-wavelength part of the spectrum, these features stretch from the central wavelength of the driver in the mid-IR all the way up to 1.5 μm [Figs. 3(b) and 4(e)]. Such a strong blueshift is never observed in near-IR filaments and becomes

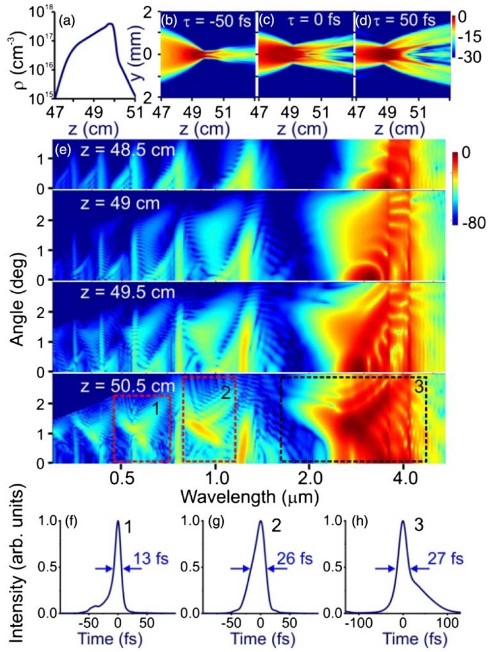

Fig. 4. (a) Longitudinal profile of the electron density in the filament. (b)–(e) Time-resolved beam dynamics calculated for different sections of the mid-infrared driver pulse, with $\tau = -50$ fs (b), –25 fs (c), 0 fs (d), and 50 fs (e). (f) Results of simulations for the angle-resolved spectra of the supercontinuum output of the filament induced by 3.9 μm, 80 fs, 17 mJ driver pulses at different points z along the filament (as specified in the panels). (g)–(i) Temporal envelopes of field waveforms corresponding to spectral regions of 450–720 nm (g), 790–1150 nm (h), and 1500–4200 nm (i), contoured by dashed lines in panel (f) at $z = 50.5$ cm, with a compensation of a linear chirp of 40 fs^2 (*g*, *h*) and with phase compensation using 3 mm of BaF_2 (i).

possible due to the λ^3 scaling of the ionization blueshift with the central wavelength of the driver λ [16]. Both the frequency shift of this off-axial component and its position within the beam agree well with the results of angle-resolved spectral measurements [Figs. 3(a) and 3(b)]. Simulations with the shock-wave term switched off in the field evolution equation show that less than 5% of blueshifting in our filamentation geometry is due to shock-wave effects.

As a part of subsequent filamentation dynamics, the central part of the driver pulse is refocused due to the Kerr nonlinearity [Figs. 4(c) and 4(d)], forming a filament in the central part of the beam. This filament emits intense supercontinuum radiation with experimentally detected spectra spanning from 250 to 6500 nm [Figs. 2(a) and 4(e)], in full agreement with experiments [Fig. 3(a)]. While reliable spectral measurements for wavelengths longer than 6.5 μm were not possible in our experiments, simulations, as can be seen in Figs. 2(a) and 4(e), suggest that the mid-IR wing of the supercontinuum spectrum extends well beyond 6.5 μm, even though it is modulated and attenuated by water absorption, yielding an overall supercontinuum bandwidth well above five octaves.

Enhanced blueshifting observed in mid-IR filaments open new avenues for the compression of high-peak power laser pulses, strengthening motivation for filamentation-based pulse compression in the mid-IR [17,18]. As can be seen from simulations presented in Figs. 4(f)–4(h), efficient pulse compression is possible within individual spectral bands filtered out of the supercontinuum output [as shown by dashed contours in Fig. 4(e)] through a simple compensation of the linear part of their chirp [Figs. 4(f) and 4(g)]. Due to the enhanced blueshift, compression to few- and single-cycle pulse widths can be achieved in the long-wavelength part of the supercontinuum spectrum through partial chirp compensation within a few millimeters of an anomalously dispersive material. In Fig. 4(h), we illustrate pulse compression of the 1.5–4.2 μm band of the supercontinuum filament output [filtered as shown in Fig. 4(e)] through partial chirp compensation in 3 mm of BaF_2, yielding a 27 fs pulse width, corresponding to 2.7 field cycles at $\lambda \approx 3.0$ μm.

Funding. Russian Foundation for Basic Research (RFBR) (14-29-07182, 16-02-00843, 15-02-08792, 15-32-20897, 16-32-60164); Welch Foundation (A-1801); Russian Science Foundation (RSF) (14-12-00772); Office of Naval Research (ONR) (00014-16-1-2578).

REFERENCES

1. A. Braun, G. Korn, X. Liu, D. Du, J. Squier, and G. Mourou, Opt. Lett. **20**, 73 (1995).
2. A. Couairon and A. Mysyrowicz, Phys. Rep. **441**, 47 (2007).
3. L. Berge, S. Skupin, R. Nuter, J. Kasparian, and J.-P. Wolf, Rep. Prog. Phys. **70**, 1633 (2007).
4. C. P. Hauri, W. Kornelis, F. W. Helbing, A. Heinrich, A. Couairon, A. Mysyrowicz, J. Biegert, and U. Keller, Appl. Phys. B **79**, 673 (2004).
5. S. Skupin, G. Stibenz, L. Bergé, F. Lederer, T. Sokollik, M. Schnurer, N. Zhavoronkov, and G. Steinmeyer, Phys. Rev. E **74**, 056604 (2006).
6. A. V. Mitrofanov, A. A. Voronin, D. A. Sidorov-Biryukov, G. Andriukaitis, T. Flöry, A. Pugžlys, A. B. Fedotov, J. M. Mikhailova, V. Ya. Panchenko, A. Baltuška, and A. M. Zheltikov, Opt. Lett. **39**, 4659 (2014).
7. J. Kasparian, M. Rodriguez, G. Méjean, J. Yu, E. Salmon, H. Wille, R. Bourayou, S. Frey, Y.-B. André, A. Mysyrowicz, R. Sauerbrey, J.-P. Wolf, and L. Wöste, Science **301**, 61 (2003).
8. D. Kartashov, S. Ališauskas, A. Pugžlys, A. Voronin, A. Zheltikov, M. Petrarca, P. Béjot, J. Kasparian, J.-P. Wolf, and A. Baltuška, Opt. Lett. **37**, 3456 (2012).
9. A. V. Mitrofanov, A. A. Voronin, D. A. Sidorov-Biryukov, A. Pugžlys, E. A. Stepanov, G. Andriukaitis, T. Flöry, S. Ališauskas, A. B. Fedotov, A. Baltuška, and A. M. Zheltikov, Sci. Rep. **5**, 8368 (2015).
10. A. V. Mitrofanov, A. A. Voronin, S. I. Mitryukovskiy, D. A. Sidorov-Biryukov, A. Pugžlys, G. Andriukaitis, T. Flöry, E. A. Stepanov, A. B. Fedotov, A. Baltuška, and A. M. Zheltikov, Opt. Lett. **40**, 2068 (2015).
11. A. V. Mitrofanov, A. A. Voronin, D. A. Sidorov-Biryukov, S. I. Mitryukovsky, A. B. Fedotov, E. E. Serebryannikov, D. V. Meshchankin, V. Shumakova, S. Alisauskas, A. Pugzlus, V. Ya. Panchenko, A. Baltuska, and A. M. Zheltikov, Optica **3**, 299 (2016).
12. D. Kartashov, S. Ališauskas, G. Andriukaitis, A. Pugžlys, M. Shneider, A. Zheltikov, S. L. Chin, and A. Baltuška, Phys. Rev. A **86**, 033831 (2012).
13. L. V. Keldysh, Zh. Eksp. Teor. Fiz. **47**, 1945 (1964) [Sov. Phys. J. Exp. Theor. Phys. 20, 1307 (1965)].
14. M. Scheller, M. S. Mills, M. Miri, W. Cheng, J. V. Moloney, M. Kolesik, P. Polynkin, and D. N. Christodoulides, Nat. Photonics **8**, 297 (2014).
15. P. A. Zhokhov and A. M. Zheltikov, Phys. Rev. Lett. **110**, 183903 (2013).
16. S. C. Rae and K. Burnett, Phys. Rev. A **46**, 1084 (1992).
17. L. Bergé, Opt. Express **16**, 21529 (2008).
18. L. Bergé, J. Rolle, and C. Köhler, Phys. Rev. A **88**, 023816 (2013).